American Mineralogist, Volume 97, pages 828–839, 2012

The morphology of the reaction front of the dissolution-precipitation reaction rutile + wollastonite = titanite in time series experiments at 600 °C/400 MPa

Friedrich Lucassen,[1,2,*] Gerhard Franz,[1,†] Richard Wirth,[2] Matthias Weise,[3] and Andreas Hertwig[3]

[1]Technische Universität Berlin, Fachgebiet Petrologie—ACK 9, Ackerstrasse 71-76, 13355 Berlin, Germany
[2]Deutsches GeoForschungsZentrum, Telegrafenberg, 14473 Potsdam, Germany
[3]Federal Institute for Materials Research and Testing, Unter den Eichen 44-46, 12203 Berlin, Germany

Abstract

Fluid-assisted mass transport reactions by dissolution-precipitation, where a precursor mineral reacts with a fluid, play an important role in metamorphism and metasomatism. We investigated titanite growth on rutile in time series experiments between one and 107 days at constant *P-T* conditions of 600 °C and 400 MPa in the system TiO_2-CaO-SiO_2-Na_2O-HCl-H_2O. A two-capsule assemblage allows for transport of Ca and Si from dissolving wollastonite to dissolving rutile, the Ti-source, in a NaCl-bearing aqueous fluid, according to the general reaction $CaSiO_3 + TiO_2 = CaTiSiO_5$. Complete overgrowth of rutile by titanite occurred after just one day of experiment. Fine-grained lozenge-shaped titanite crystals of short-time runs (up to 14 days) reorganize to larger predominantly prismatic crystals after >14 days.

After investigation by scanning electron microscopy, the titanite overgrowth was removed from the rutile by hydrofluoric acid, to provide a three-dimensional view of the dissolution-reaction front on the rutile surface. The morphology of the rutile surface is dominated by humps or ridges beneath the central region of a titanite crystal and valleys at the grain boundaries between adjacent titanite crystals. The dissolution pattern on the rutile surface mimics the titanite overgrowth and changes with changing grain size and shape of the titanite with longer run times. The preferred dissolution of rutile in the valleys is clearly linked to the position of the titanite grain boundaries, which served as pathways for fluid-assisted element transport. Rutile-titanite and titanite-titanite boundaries show a significant porosity in transmission electron microscopy images of foils prepared by focused ion beam milling. The large-scale dissolution pattern on the rutile surface is independent of the crystallographic orientation of the rutile and entirely dominated by the arrangement of titanite crystals in the overgrowth. Dissolution features on a scale smaller than ~1 µm are dominated by stepwise dissolution and etch-pits following the crystallographic orientation of the rutile. Similar observations were made in experiments with an additional Al-source, although these experiments result in a different overgrowth pattern; i.e., an exposed rutile surface is always present and solitary titanite crystals are accompanied by partial overgrowths. Quantitative characterization of the surface morphology by white-light interference microscopy demonstrates that, with increasing grain size of titanite, dissolution of rutile is strongly enhanced at the titanite grain boundaries.

Natural examples of titanite overgrowths on rutile show the same relations between element pathways, arrangement of titanite crystals and 3D dissolution pattern on rutile as in the experimental systems. We conclude that the transport of Ti away from the rutile and of Ca + Si into the reaction rim occurred in a grain boundary fluid, the composition of which must have been strongly different from the composition of the bulk fluid in the experiment, as well as in the natural system. The reaction progress depends on the availability of a fluid, and relicts of rutile in titanite indicate restricted availability of fluid in the natural system (e.g., a fluid pulse that was consumed by the reactions). The reaction examined here can serve as a proxy for other reactions of the conversion of oxide minerals (e.g., spinel or corundum) into silicates.

Keywords: Experimental mineralogy, rutile, titanite, dissolution-precipitation, reaction morphology

Introduction

The mechanism of many reactions in metamorphic rocks is a dissolution-precipitation process. If sufficient fluid is available, and if the fluid is not in equilibrium with the solid phase assemblage, the minerals will react forming the stable phase (Putnis 2009). Typical features of such reactions are reaction coronas or rims around the precursor mineral, often resulting in pseudomorphs if the reaction is volume conservative. Another typical feature of such reactions is the formation of porosity that facilitates fluid flow and allows material transport for efficient reaction progress because solid-state diffusion is slow for many minerals at low temperatures. The reaction produces a front between two minerals,

* Present address: Isotope Geochemistry Group, Department of Geosciences, MARUM Center for Marine Environmental Sciences, University of Bremen, 28334 Bremen, Germany.
† E-mail: gerhard.franz@tu-berlin.de

0003-004X/12/0506–828$05.00/DOI: http://dx.doi.org/10.2138/am.2012.3742

and its shape is critical for exploration of the pathways for material transport in a fluid-mediated reaction. Many experiments in several systems and investigations in natural rocks have revealed the morphology of reaction coronas in two-dimensional sections, but their geometry in three dimensions has not yet been explored.

Titanite ($CaTiSiO_5$) growth at the expense of rutile (TiO_2) is a characteristic phenomenon during retrogression of granulites, calc-silicate rocks, and eclogites, as shown by the common occurrence of monomineralic titanite coronas around rutile relicts (e.g., Brewer et al. 2003; Rötzler et al. 2004; Lucassen et al. 2010a). Pseudomorphic replacement of rutile by titanite is commonly not observed and also not expected; such a process would require substantial sequestration of Ti by the fluid and deposition away from the reaction site, because the molar volume of titanite (55.7 cm^3/mol) is approximately three times that of rutile (18.8 cm^3/mol). Corona textures range in scale from incipient, micrometer-thick rims to macroscopically visible titanite crystals with small rutile relicts. Titanite reaction rims are monomineralic, and transport of Ca+Si through the reaction rim toward rutile and of Ti from the rutile must have occurred, at least on the grain scale. Therefore, actual titanite formation presumably takes place as a fluid-assisted mass transport reaction. One can distinguish two extreme scenarios. (1) If Ti-transport is rapid, the rim will grow on the outer side of the titanite overgrowth (Fig. 1a). Pathways must exist to transport Ti from the rutile-titanite to the titanite-bulk fluid interface, where it can be combined with Ca and Si. (2) If Ti-transport is slow compared to that of Ca and Si, the rim will grow at the rutile-titanite interface and pathways for Ca and Si to the inner reaction front must exist.

The present experimental study explores patterns of titanite growth on rutile and the related dissolution patterns on the surface of the rutile according to the general reaction $CaSiO_3 + TiO_2 = CaTiSiO_5$. We provide a 3D image of the dissolution front and its morphology on the rutile, made visible by dissolution of the titanite overgrowth in hydrofluoric acid (HF). Time series experiments, including 1, 3, 7, 14, 30, 60, and 107 days in the system TiO_2-CaO-SiO_2-Na_2O-HCl-H_2O, were performed at constant *P-T* conditions of 600 °C and 400 MPa. We used a double-capsule technique, where a rutile crystal, serving as a source of Ti, is physically separated from wollastonite, delivering Ca and Si, and all element transport occurs via a NaCl-brine (Fig. 1b). Wollastonite represents the most simplified case of a rock matrix. We compare the growth patterns exhibited by titanite crystals produced at the same *P-T* conditions in the present work (referred to as the "Al-free system") and the previously investigated experimental system containing Al ± CaF_2 ("Al-system"; Lucassen et al. 2010b). The morphology of titanite overgrowth and dissolution patterns on rutile was studied by scanning electron microscopy (SEM). The morphology of dissolution patterns on an originally polished surface of a synthetic rutile crystal was characterized quantitatively by white-light interference microscopy. Internal microstructures of possible open pathways for element transport at the titanite-titanite and rutile-titanite interfaces were studied with SEM and transmission electron microscopy (TEM) using the focused ion beam (FIB) preparation method. These data were combined with images of the titanite overgrowth in polished sections and of the titanite-fluid interface to derive a conceptual model of the relation between titanite growth and rutile dissolution with time.

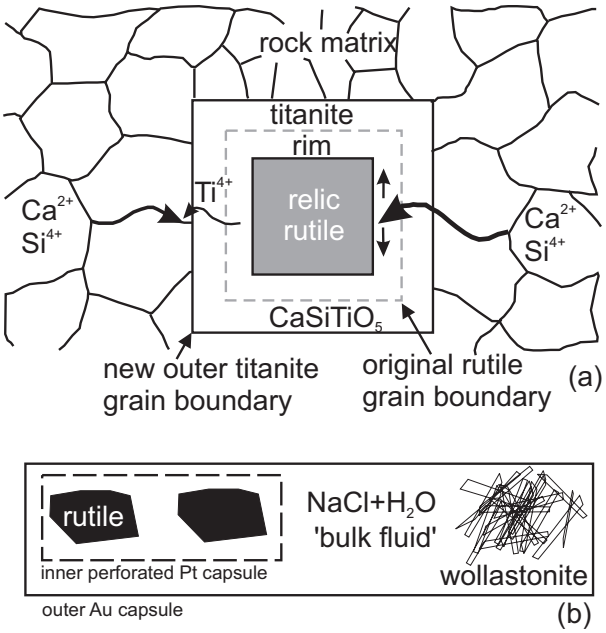

FIGURE 1. (**a**) Scheme of growth of a titanite rim around rutile in a rock matrix. Transport of Ca + Si to the inner reaction front (right) and/or Ti to the outer reaction front (left) occurs in a fluid phase. (**b**) Experimental setup for the growth of titanite from rutile. The starting rutile crystals are physically separated from wollastonite by a perforated Pt capsule (2.5 mm diameter) with pathways for the bulk fluid, a highly concentrated NaCl-solution. Rutile crystals were on the order of ~1 mm in size; wollastonite was crushed to a grain size of <1 mm. The whole assembly was placed in an outer Au tube (Ø 5 mm) approximately 3 cm in length.

EXPERIMENTAL METHODS

All experiments were run with the same experimental settings as those used previously for the Al-system (Fig. 1b) and with the same starting materials, i.e., a pure wollastonite from a contact metamorphic rock and a pegmatitic rutile with <1 wt% Fe_2O_3 (see Lucassen et al. 2010b for more details). For comparison, our series of experiments included one run with a synthetic rutile crystal (RT41; Table 1). This single crystal of rutile (grown by the flame fusion method; SurfaceNet GmbH, Rheine, Germany) was crystallographically orientated and high-grade polished on the (110) face. The other ingredients were analytical grade NaCl and distilled H_2O, added in a weight-ratio of 1:1 ($X_{H_2O} \approx 0.76$) to produce a highly concentrated, but not supersaturated, fluid at run conditions. The activity of H_2O in the H_2O-NaCl system is ~0.66 at run conditions (Aranovich and Newton 1996), but might be further influenced by Ca and Si in the solution. Solubility of rutile in pure H_2O is very low (e.g., Tropper and Manning 2005; Antignano and Manning 2008), especially in comparison with the solubility of wollastonite in H_2O (Fockenberg et al. 2006; Newton and Manning 2006). The addition of NaCl enhances the solubility of wollastonite (Newton and Manning 2006) and of rutile (Rapp et al. 2010), which is seen in the enhanced titanite growth compared with exploratory experiments using pure H_2O.

The mixture was loaded into an Au capsule, a Pt capsule with the rutile was placed on top, then the Au capsule was sealed by arc welding and placed in an oven at 110 °C to check for tightness. The capsules were then placed in externally heated cold-seal vessels, pressurized by water to 400 MPa, and heated under controlled pressure to 600 °C. The automatic temperature control keeps temperature constant within ±10 °C at hydrothermal laboratories at Technische Universität Berlin and Deutsches GeoForschungszentrum Potsdam. Checks of the pressure during the experiment were within the reading-precision of ±10.0 MPa. The vessels were quenched in an air stream to room temperature within 5 min, while maintaining the pressure. The pH values of the extracted solution after the experiment and the distilled H_2O used in the experiments are the same from estimates with pH sensitive indicator paper.

Representative run products were investigated by TEM, using FIB sample

TABLE 1. Run data for the experiments at constant *P-T* conditions of 400 MPa and 600 °C

Run	Run time (days)	Wollastonite (g)	Rutile (g)	Fluid H_2O-NaCl* (g)	Grains/mm^2
Ttn6	1	0.0445	0.0359	0.0831	7200
Ttn11	3	0.0454	0.0328	0.0871	2730
RT4	7	0.0190	0.0240	0.0490	n.d.
Ttn5	7	0.0325	0.0241	0.0698	920
RT26	14	0.0382	0.0431	0.1800	900
RT8	30	0.0559	0.0420	0.0601	n.d.
RT14	30	0.0133	0.0173	0.0550	870
RT41†	30	0.0220	0.0117	0.0956	n.d.
RT18	60	0.0424	0.0205	0.1114	910
RT21	107	0.0622	0.0287	0.1148	900

Note: Number of grains/mm^2 were counted on titanite overgrowths after run; run product is a complete titanite overgrowth; n.d. = not determined.
* The fluid contains ~50 wt% NaCl except run RT8 with 20 wt% NaCl.
† Synthetic rutile, all others natural rutile. This run contains additionally 0.0075 g of Al_2O_3.

preparation with a FEI FIB200TEM device. Electron-transparent foils with the typical dimensions $15 \times 10 \times 0.150$ µm were cut from selected areas of a polished thin section. Details of the FIB milling are given in Wirth (2004, 2009). TEM investigations were performed with a FEI TECNAI F20 X-Twin instrument incorporating a field emission gun operated at an accelerating voltage of 200 kV, and equipped with a Gatan imaging filter (GIF, Tridiem), an EDAX X-ray analyzer with an ultra-thin window, and a Model 3000 high-angle annular dark field detector (Fischione Instruments). Bright-field and dark-field images usually were acquired as energy filtered images applying a 20 eV window to the zero loss peak.

For selected experiments, the titanite overgrowth was subsequently removed in warm HF to uncover the shape of the reaction front on the rutile. The progress of dissolution was controlled under the binocular microscope. The overgrowth was completely removed after 2–4 h. After cleaning the rutile grains in an ultrasonic bath, only very few patches of CaF_2 remained on the surface of the rutile. In X-ray maps, the rutile surfaces showed only TiO_2. Neither films nor relicts of other phases were found. To check if HF damages the rutile surface, we compared SEM images of rutile boiled in hot HF with those of untreated rutile. Both show essentially the same surface morphology. The comparison was also made with polished pieces of synthetic rutile. The submicrometer-sized polishing scratches were not influenced by HF. Because boiling in hot HF does not significantly affect the rutile, we consider the features observed on the rutile surface after titanite dissolution in warm HF to have been induced by the titanite-forming reaction.

The morphology of the dissolution front imparted on the polished surface of synthetic rutile RT41 was measured by white light interference microscopy using a NewView 5022 (ZygoLOT) instrument and Truemap software (version 5.2.13) for data evaluation. The spatial resolution in the x-y plane is 500 nm, limited by the lens magnification of 50×, whereas in the z-direction (depth), it is better than 10 nm. The system was calibrated prior to the measurements with a 1.8 µm step height standard to ensure the accuracy of absolute z values.

RESULTS

Al-free system

Run conditions and weights of the starting materials and fluid phase are listed in Table 1. The reaction never went to completion; rutile and wollastonite remain present in all runs, but already after the shortest run of one day, a complete overgrowth of titanite formed on rutile (Fig. 2a). The only new mineral formed is titanite of stoichiometric composition $CaTiSiO_5$ as determined by electron microprobe. Titanite exclusively grew around the rutile and was never detected as solitary grains in or outside the inner capsule, indicating negligible transport of Ti out of the inner capsule. The same observation was made earlier for the Al-system by Lucassen et al. (2010b). In some experiments, fracturing of the rutile occurred with voluminous titanite growth along undetected cracks in the starting rutile, probably in a self-accelerating process, facilitated by the large molar volume of titanite. These samples are not considered here. Irregularly distributed spheres of quench products on the surface of the titanite contain Si, Ca, variably low Na, but no Ti detectable by SEM-based EDX. The overgrowth pattern changes with run duration (Figs. 2a–2c), and involves coarsening of the grains, changes in crystal habit and the arrangement of crystals. Lozenge-shaped crystals are first arranged in a floral pattern, where several crystals radiate from a nucleation center (Figs. 2a and 2b). The number of titanite grains per unit area vs. run duration decreases rapidly and approaches a near-steady state after seven days (Fig. 2i; Table 1). The prevailing crystal shape is still a lozenge in the seven- and 14-day runs, but the crystal size is larger compared with the one- and three-day runs (Fig. 2i). In runs lasting 30 days or more, the floral structure disappeared, giving way to dominantly prismatic crystals (Fig. 2c), but the average crystal size did not increase (Fig. 2i). Euhedral titanite grew into the fluid and newly nucleated small titanite grains occur on the surface of large titanite grains even after a long run time of 107 days. This indicates transport of Ti through the titanite rim and its immediate fixation with Ca and Si at the titanite-fluid interface. Preferred growth of titanite on specific crystal faces of the host rutile is not observed.

After short runs (1–14 days), titanite overgrowth largely restricts to a single layer of crystals on the rutile. In the longer runs, growth of titanite on titanite is common, but no continuous second layer of titanite crystals has formed. In 2D-sections, the grain boundaries between titanite and rutile are cuspate, with narrow "valleys" of titanite and "humps" of rutile beneath the titanite crystals (Figs. 3a and 3b).

Observations on polished grain mounts under reflected light and the SEM reveal closed titanite-rutile and titanite-titanite boundaries, but also significant porosity below the titanite overgrowth in rutile, as well as between titanite crystals in the overgrowths (Figs. 3d and 3e). TEM investigations of rutile-titanite and titanite-titanite boundaries in six FIB-cut foils confirm that most of these boundaries are closed and show no porosity (not shown). However, others are open with a width of less than ~200 nm, and show porosity (Figs. 3f and 3g). The pores are devoid of trapped fluid (NaCl), reaction products, or amorphous phases. In the Al-system, observations on TEM foils revealed similar features, but pores filled with NaCl-crystals were found (Lucassen et al. 2010b; their Fig. 7d). In run RT21 (107 days), we observed growth of a spongy titanite aggregate (confirmed by X-ray element mapping) into the rutile beneath a titanite-titanite boundary (Fig. 3e). The boundary between the spongy titanite and rutile is irregular and indicates further dissolution and reaction.

After removing the titanite overgrowth with HF, it is obvious that the growth of titanite had re-sculptured all faces of the rutile (Figs. 2d–2f). Patterns controlled by the crystallographic orientation of titanite crystals in the overgrowth did not develop on the rutile, but steps and striations parallel to the *c* axis of the rutile are still visible (Fig. 2d). In the short-time experiments, the traces of titanite on the rutile surface repeat the pattern observed at the surface of the titanite overgrowth, e.g., the lozenge-shape of titanite crystals and their arrangement in a radiating floral pattern (Fig. 2). Considering the preservation of the geometry of the overgrowth, we can locate the central region of a dissolved titanite grain and the region of contact between adjacent grains. The revealed surface pattern is consistent and comprises a hump (or ridge in the case of elongate titanite crystals) in the central region and an incised

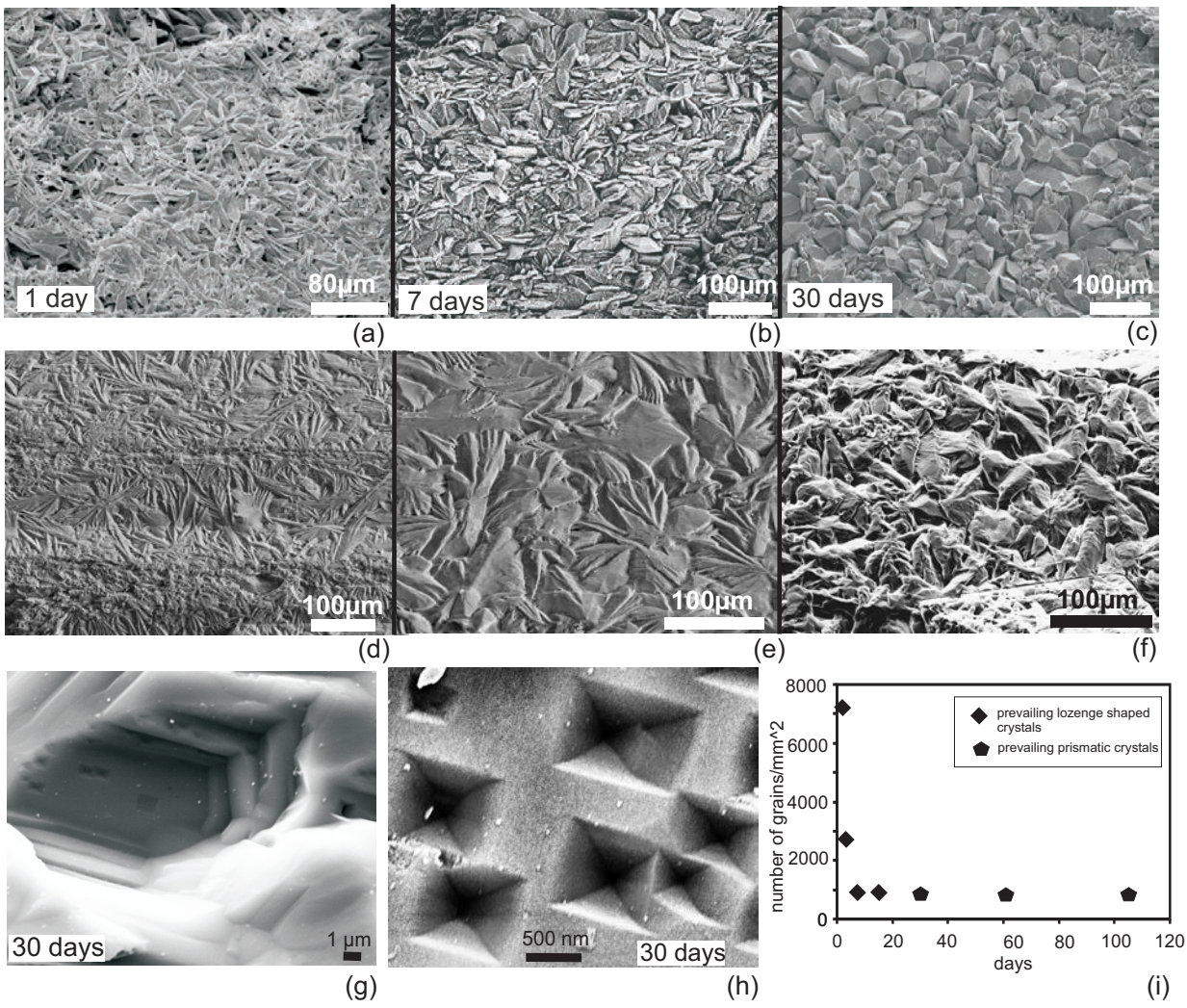

FIGURE 2. (**a**–**c**) SEM images of titanite overgrowth on rutile for different run durations; (**d**–**h**) morphology of the corresponding rutile surfaces after removal of the titanite overgrowth, which mimics the titanite morphology with a hump-and-valley texture. (**a**) One-day run (ttn6); the overgrowth is already complete with typical lozenge-shaped titanite crystals in random orientation. (**b**) Seven-day run (ttn3); crystals are coarser and many are arranged in a floral pattern with several crystals radiating from a center. (**c**) Thirty-day run (RT14); grain shapes are dominantly prismatic due to coarsening; floral patterns disappeared. (**d**) Small grain size of titanite is imprinted on the rutile surface. Floral patterns are more pronounced, whereas linear patterns are inherited from the precursor rutile surface with striations and steps parallel to the *c* axis. No correlation between the dissolution pattern and the crystallographic orientation of the rutile is observed. (**e**) Titanite grain coarsening with increasing run duration; floral patterns are typical. (**f**) Prismatic crystal shape is imprinted on the rutile; humps and cavities become more pronounced with run time. (**g**) Cavities on the rutile surface (run RT14 and other long-time runs) are commonly terraced and show smaller etch-pits. (**h**) Etch-pits occur exclusively on planar features at the bottom and terraces in the cavities. (**i**) Number of titanite crystals per unit area with run time. For run times up to 14 days, lozenge-shaped crystals dominate. We distinguish short-time (≤14 days) from long-time (≥30 days) runs by the predominance of lozenge or prismatic crystal shapes.

valley along the contact between two titanite crystals (Fig. 2). This hump-and-valley pattern is common at the grain scale to all otherwise different overgrowth patterns. Large etch-pits with a size of >1 µm (up to a few micrometers) and a regular outline on the rutile surface are scarce. In the long-time experiments, the rutile surface evolves with the evolving titanite pattern. In the 30-day experiment, the above-described floral clusters have disappeared and much coarser humps are defined by the valleys (Fig. 2f). Next to the still dominant hump-and-valley texture, etch-pits with a regular outline are deeper and commonly descend stepwise to a flat bottom (Figs. 2g and 2h). Their size is variable and ranges from a few to ~40 µm along their long axis. The flat-bottomed areas and some steps host pyramidal etch-pits, which commonly form squares, less commonly rectangles ranging in size from ~200 nm to 1 µm with 90° intersect between pit-walls (Figs. 2g and 2h).

Al-system

Titanite in the Al-system (which is Si undersaturated) shows different growth behavior under identical *P-T-t* conditions (details in Lucassen et al. 2010b). There is no difference between natural

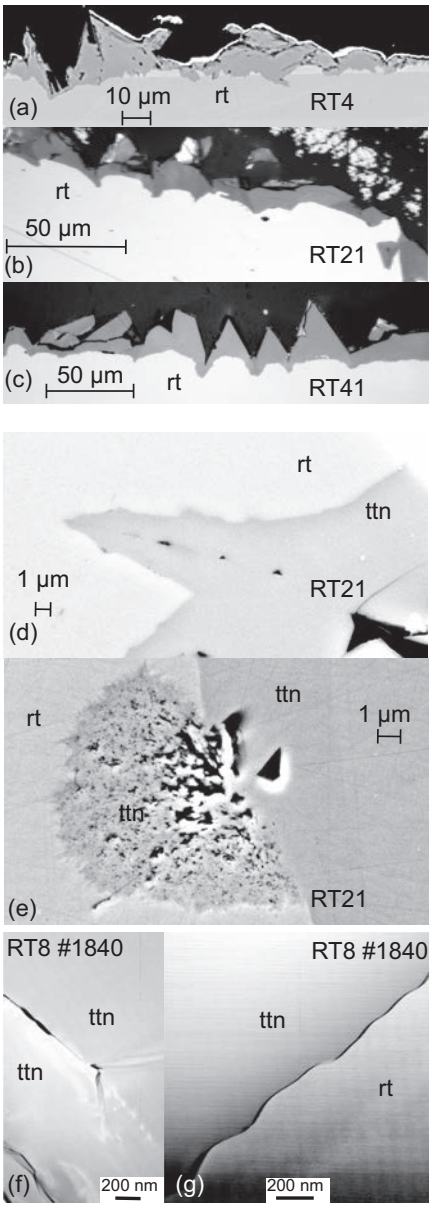

Figure 3. (**a**) Hump-and-valley morphology on the rutile surface (SEM image; natural rutile as starting material). Valleys are located beneath the titanite grain boundaries, whereas humps are beneath the center of titanite grains. The white discontinuous layer on rutile is also rutile but with a higher Fe-content. (**b**) Grain boundaries between titanite, revealed by variations in reflectance owing to the different orientation of titanite crystals (reflected-light optical microscopy). (**c**) Hump-and-valley morphology on the polished precursor (110) face of synthetic rutile; the valleys are located beneath the grain boundaries between the titanite crystals. (**d**) Porosity along a titanite-titanite grain boundary; the titanite crystals fill a valley in the rutile (SEM image). (**e**) Spongy titanite aggregate extending beneath a titanite-titanite boundary into rutile. The irregular pattern of the rutile-titanite contact could be related to the occurrence of etch-pits (SEM; cf. Figs. 4g and 4h). (**f**) Partly open titanite-titanite grain boundaries. TEM image (HAADF detector). (**g**) Partly open rutile-titanite boundary; note that closed grain boundaries are more common. TEM image (HAADF detector). Selected data from six-day (RT4), 30-day (RT8 and RT41), and 107-day (RT 21) runs.

and synthetic starting rutile (see run RT41). Growth starts with solitary grains on the rutile surface and even after long-time runs, the rutile surface is not completely overgrown. We selected two grains from long-time experiments for removing the titanite (RT19 and RT20; natural rutile, 107 days; Lucassen et al. 2010b). One grain has a large exposed rutile surface, which was the rutile-fluid interface during the experiment (run RT20; Figs. 4a–4d) and the second is largely covered by titanite (Figs. 4e–4h). Where solitary, large titanite crystals rested on the rutile surface (Fig. 4a), the terraced slope of the hump merges either into the exposed rutile surface (Fig. 4b), or humps are surrounded by shallow trenches formed below the crystal (Fig. 4c). Small-scale dissolution patterns beneath some titanite crystals are similar to those observed in the Al-free system (Fig. 4d). On the exposed rutile surface, progress of dissolution is rather uniform and emphasizes the pre-existing striation parallel to the *c* axis on the different crystal faces (Figs. 4a and 4b).

The hump-and-valley texture observed in the Al-free system is also present in the Al-system, where the titanite grains are connected to form a partial overgrowth. A polished section through such a rutile rim is shown in Figure 3c (run RT41, 30 days). The overgrowth of coarse-grained titanite from run RT19 (Fig. 4e) is associated with an impressive imprint on the rutile surface revealed after dissolution of the titanite (Fig. 4f), where a network of trenches formed at the bottom of the incised valleys (Fig. 4f). Dissolution features, which penetrate into the rutile crystal, form cavities with an irregular outline, mostly in the trenches, but also in areas near the trenches, rarely on the humps (Figs. 4f–4h). The trenches mark the location of the former titanite-titanite interfaces. Transitions between the valleys and trenches are sharp; these trenches comprise numerous cascades of steps confining flat-bottomed rectangular cavities (Figs. 4g and 4h). Within the cavities, dissolution formed a network of etch-pits leaving only a framework of rutile on the scale of a few micrometers to <100 nm. Because of the Pt-coating, higher magnification did not reveal any further detail. Surface views of the titanite overgrowth on synthetic rutile from run RT41 (Fig. 5a), the rutile surface (Fig. 5b), the quantified morphology of the rutile surface obtained from white light interference microscopy (Fig. 5c), and elevation profiles across the map (Fig. 5d) enable direct comparison of the differences caused by dissolution on the rutile surface beneath the areas with fine-grained and coarse-grained titanite. The observed difference between the deepest cavity and highest peak is 57 µm. Such extreme amplitudes are rare, however. Profiles across the rutile surface beneath relatively fine-grained and coarse-grained titanite (profiles A and B, respectively) show an average amplitude of ~15 and ~30 µm, respectively. The average valley-peak wavelength is also smaller beneath the fine-grained titanite in comparison with coarse-grained titanite (~50 and ~130 µm, respectively).

Discussion

Solubility of the educt phases

The exclusive formation of titanite around the Ti source, the rutile, and the absence of Ti phases in the outer capsule at the wollastonite, indicate that only very minor Ti was incorporated into the bulk fluid. This is interpreted as evidence of strong immobility of Ti relative to Ca and Si (and Al in the Al-system), which is consistent with available data on rutile solubility (Ayers and

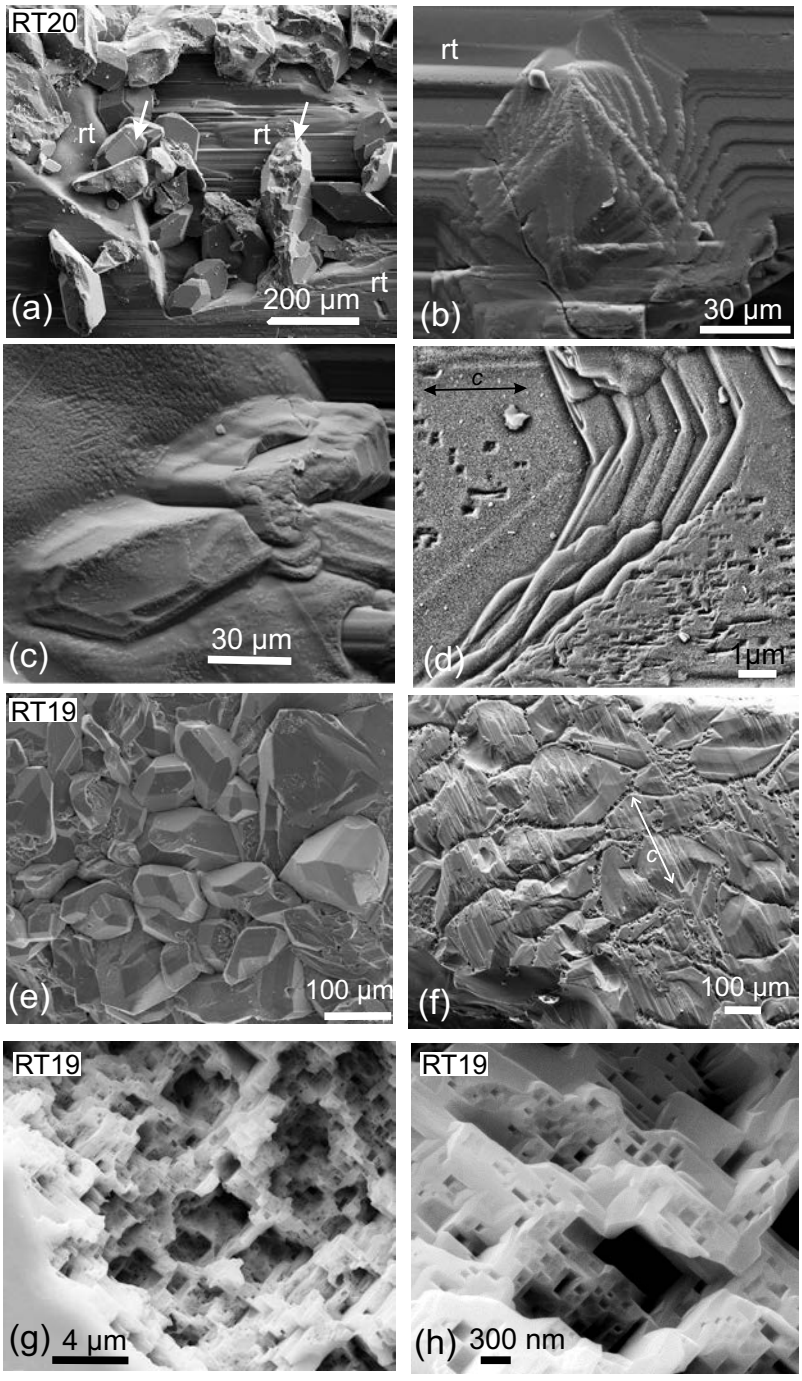

Figure 4. SEM images of titanite overgrowth patterns and large- and small-scale dissolution patterns on the rutile surface after dissolution of the titanite with HF; 107-day runs RT19 and RT20 in the Al-system (run data in Lucassen et al. 2010). (**a**) Rutile (Rt), only partially overgrown by titanite (arrows). (**b**) Rutile surface (Rt) beneath a dissolved titanite crystal (right arrow in **a**), now an elevated rutile surface with a terrace-like dissolution pattern. Pronounced striation and steps parallel to the *c* axis on the rutile allow the precise location of the dissolution sculpture to be determined. (**c**) Rutile surface (left arrow in **a**) smoothed by dissolution. (**d**) Contrasting dissolution pattern of rutile dominated by the crystal shape of the monoclinic titanite (steps) and etch-pits with an outline following the crystallographic orientation of the rutile (*c* direction indicated by double-head arrow). (**e**) Polycrystalline titanite overgrowth and (**f**) the trace of the titanite grain boundaries on the same rutile surface after removal of the titanite with HF; exact location unknown. The *c* direction of rutile (indicated by double-head arrow) is shown by striations. Between large titanite crystals, deep trenches formed in the valleys by dissolution (upper arrow head). (**g**) Small-scale dissolution patterns, dominated by the tetragonal symmetry of the rutile, showing the sharp transition of a valley (smooth area at lower left near the label) into a trench, consisting of a relict rutile framework (compare Fig. 3e). (**h**) Tetragonal etch pits in the rutile framework.

Watson 1993; Audétat and Keppler 2005; Tropper and Manning 2005; Antignano and Manning 2008; Manning et al. 2008; Rapp et al. 2010). Although the results of these solubility studies strongly differ in absolute amounts of rutile dissolution and applied *P-T-x*-conditions, they agree overall that the solubility of rutile is low.

The congruent dissolution of wollastonite and possible complexation of Ca and Si in a NaCl-brine were described by Newton and Manning (2006) as $CaSiO_3 + NaCl + 2H_2O = CaCl^+ + OH^- + H_3NaSiO_4$. Dissolution experiments on rutile (0.5 GPa; Rapp et al. 2010) and wollastonite (1 GPa; recalculated from Eq. 4 of Newton and Manning 2006) at 800 °C in a brine with 10 wt% NaCl indicate more than an order of magnitude higher solubility of wollastonite (~20 000 ppm $CaSiO_3$) relative to rutile (~1000 ppm Ti). The potential availability of Ca and Si in the bulk fluid is much higher than that of Ti. This is confirmed by the composition of quench products on the titanite and rutile surfaces that contain Ca and Si (and Al in the Al-system) but no detectable Ti. The growth of new wollastonite (and corundum in the Al-system) at

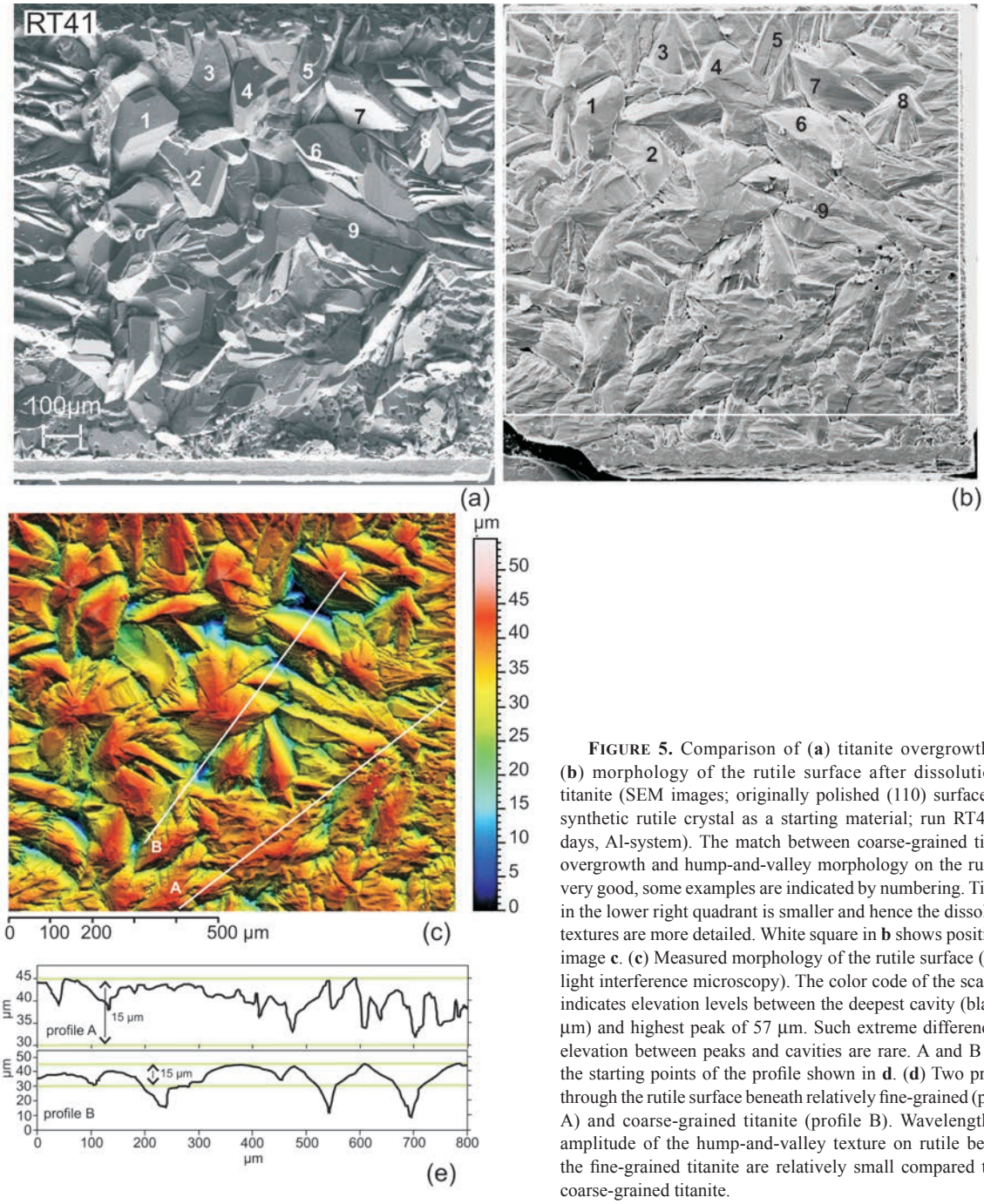

Figure 5. Comparison of (**a**) titanite overgrowth and (**b**) morphology of the rutile surface after dissolution of titanite (SEM images; originally polished (110) surface of a synthetic rutile crystal as a starting material; run RT41, 30 days, Al-system). The match between coarse-grained titanite overgrowth and hump-and-valley morphology on the rutile is very good, some examples are indicated by numbering. Titanite in the lower right quadrant is smaller and hence the dissolution textures are more detailed. White square in **b** shows position of image **c**. (**c**) Measured morphology of the rutile surface (white light interference microscopy). The color code of the scale bar indicates elevation levels between the deepest cavity (black, 0 µm) and highest peak of 57 µm. Such extreme differences in elevation between peaks and cavities are rare. A and B mark the starting points of the profile shown in **d**. (**d**) Two profiles through the rutile surface beneath relatively fine-grained (profile A) and coarse-grained titanite (profile B). Wavelength and amplitude of the hump-and-valley texture on rutile beneath the fine-grained titanite are relatively small compared to the coarse-grained titanite.

the wollastonite (and corundum) reservoir supports the assumption that the bulk fluid was near the saturation level. Therefore, we consider the bulk fluid outside the titanite reaction rim as Ca- and Si- (or Al-) saturated.

Reactions at the interfaces

Different types of phase interfaces developed during the growth of the titanite rim (Figs. 1 and 6). Three major interface types are those between titanite and rutile, titanite and fluid, and titanite and titanite. The rutile-fluid interface is transitional, because titanite separates rutile from the Ca- and Si-saturated bulk fluid after just one day of experiment; in the Si-undersaturated Al-system, the rutile-fluid interface persists throughout the entire series of experiments. The Al-free system is considered as a prototype system, in which titanite grows at the titanite-rutile and at the titanite-bulk fluid interfaces. Two extreme scenarios can be envisioned for the location of the titanite-forming reaction. (1) All dissolved Ti remains at the site of dissolution (i.e., the titanite-rutile interface), where it is incorporated in the titanite. The volume increase at the titanite-rutile interface must be compensated by strain in the titanite lattice, causing expansion of the overlying titanite overgrowth. However, plastic deformation of titanite in rocks is exceptionally rare (Müller and Franz 2004). If a ductile rock matrix is present, titanite, as an accessory phase, behaves rigidly. Therefore, we assume that during the experiment in the ductile Au-Pt capsules, titanite also behaved rigidly. Obvious deformation patterns such as mechanical twin lamellae or high dislocation density were not found in the TEM studies in the present study. Therefore, (2) the second scenario, where titanite growth at the rutile-titanite interface compensates only for the volume occupied by the dissolved rutile, is more plausible. This requires transport of ~2/3 of the dissolved Ti from the rutile-titanite interface to the titanite-bulk fluid interface, where Ti reacts immediately to form titanite. We distinguish between the bulk fluid, which approaches Ca, Si, and Al saturation but is nearly devoid of Ti (because all Ti is consumed close to its source in the titanite corona), and element concentrations in a fluid during transport along grain boundaries. The exact mechanism of transport along the grain boundaries, the exact nature of this fluid and the speciation of Ca, Si, Al, and Ti are not known. In a perfectly dry environment, volume diffusion or grain boundary diffusion are much too slow to produce large reaction rims. This has been shown in many experiments, although in systems different from the one studied here. It is also known that minute amounts of water significantly enhance this type of reaction (e.g., Joachim et al. 2011). The process, where dissolved Ti from the rutile-titanite interface is transported to the titanite-bulk fluid interface and reacts immediately to form titanite, is dominant in our experiments. Indeed, growth of euhedral titanite into the bulk fluid and increase of grain size and thickness of the titanite rim with run time require substantial transport of Ti to the titanite-bulk fluid interface.

The titanite-titanite grain boundaries change their position with time. The initially abundant small titanite crystals coarsen quickly and reorganize from thin, lozenge-shaped crystals to stubby prismatic crystals (Fig. 2). This morphological change requires grain-boundary migration, which is a common process of recrystallization in monomineralic materials.

Surface sculpture on the rutile and pathways of element transport

Dissolution of a mineral can be considered as negative growth, and thus on an atomic scale, dissolution is governed by the removal of atoms preferentially at kinks and edges (e.g., Lasaga 1995), and therefore is crystallographically controlled. At a scale of less than ~1 μm, dissolution patterns on rutile are strongly related to its structure (Figs. 3 and 4). However, on a scale larger than a few micrometers, the pattern is completely independent of the crystallographic orientation. The following discussion applies to this scale, where dissolution patterns are governed by the growing new phase. The strong connection between the titanite overgrowth pattern and the pattern of differential dissolution on the rutile is evident.

For the case of a continuous titanite overgrowth, reshaping of the rutile surface below the titanite by progressive dissolution of rutile, titanite-titanite grain-boundary migration, and concomitant formation of new titanite at the titanite-rutile and titanite-bulk fluid interfaces are summarized in Figure 6a. Dissolution-precipitation is quick and evolves on a short timescale (between one and 107 days). The valleys in rutile are preferentially located beneath titanite grain boundaries (Figs. 2–5) and the correlation of the hump-and-valley texture on rutile with the changing distribution pattern of the titanite crystals clearly indicates that the central region of the covering titanite crystals corresponds to humps, whereas the contacts between two adjacent titanite grains coincide with valleys. Dissolution of rutile beneath titanite grain boundaries decreases with distance from these boundaries along the titanite-rutile interface. The quantification of the surface morphology (Fig. 5) shows that with increasing size of titanite crystals, dissolution of rutile is strongly enhanced at the titanite grain boundaries. At the contact between the largest titanite grains obtained in our experiments, the valleys beneath these boundaries extend up to 57 μm into the rutile, whereas at the contact between small titanite grains, they do not penetrate beyond 15 μm.

Element transport from and to the rutile-titanite interface is controlled by the permeability of the titanite rim. Because porosity within the titanite grains was not observed either in microscopic or in TEM studies, we rule out this possibility; it would also contradict the slow dissolution of rutile beneath the center of titanite crystals. Open grain boundaries or porosity at rutile-titanite and titanite-titanite interfaces indirectly prove the permeability (Fig. 3). Amorphous phases, which could indicate fluid-enhanced diffusion along interfaces (e.g., Keller et al. 2006), were observed by TEM in one case at a rutile-titanite interface in the Al-system (Lucassen et al. 2010b). The increasing abundance of deeper cavities with etch-pits in the longer runs and the deep valleys observed at the contacts of coarse-grained titanite crystals could indicate the increasing importance of locally fixed element transport and therefore a stable geometry of the transport pathway. In summary, these observations and inferences require average uniform transport capacities and permeability along the titanite-titanite grain boundaries during the experiments. Considering the sparse direct observation of potential transport paths in TEM and SEM images, these could have been transient or partially destroyed during quenching. The element distribution in the bulk fluid in the capsule and the fluid along the pathways between the

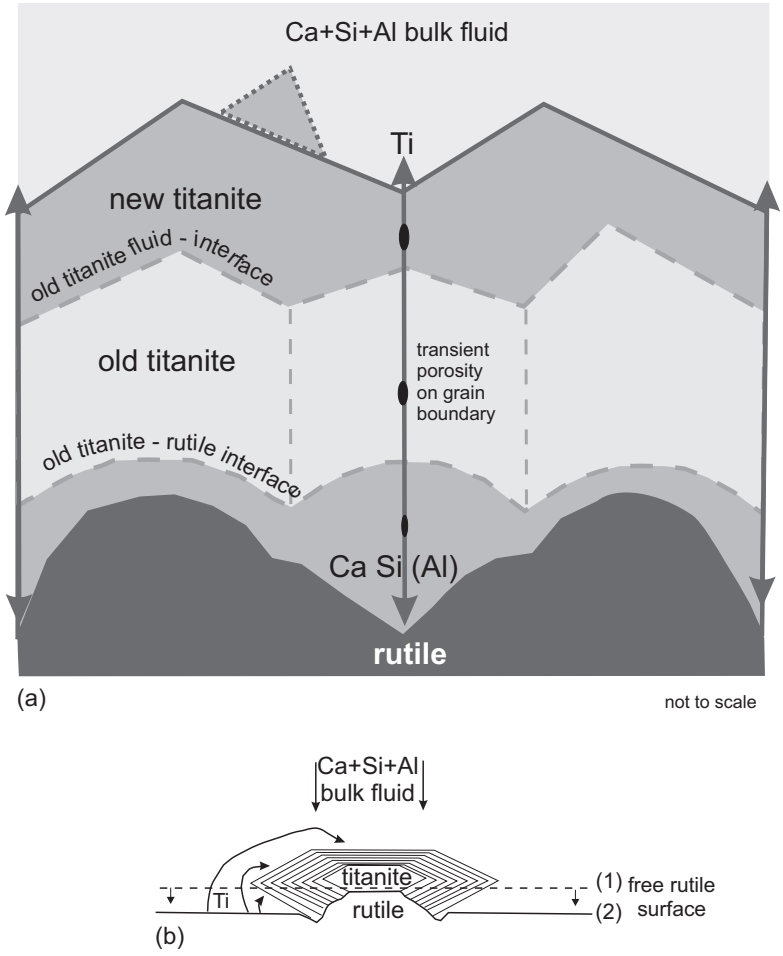

FIGURE 6. Conceptual model for progressive titanite growth, shaping the dissolution-precipitation front. (**a**) Overgrowth of titanite on rutile evolves by migration of the interfaces between rutile-titanite, titanite-titanite, and titanite-bulk fluid, which produces the characteristic hump-and-valley pattern. Two growth stages, 1 and 2, are shown (dashed lines correspond to "old titanite" and solid lines to "new titanite"); the central crystal is consumed by the other crystals through grain boundary migration. Concomitant growth of titanite occurs by dissolution of rutile mainly in the vicinity of titanite-titanite boundaries. Material transport, indicated by thick arrows, occurs along titanite grain boundaries. Titanium is efficiently transported to the titanite-fluid interface, where it also leads to the nucleation of new titanite crystals (indicated by a small crystal with stippled lines). Preferential dissolution of rutile occurs beneath titanite grain boundaries and one possible pathway for material could be transient porosity at the grain boundaries. (**b**) In the case of solitary titanite crystals (Al-bearing system) the Ti is derived by dissolution at the exposed rutile surface. The migration of the rutile-fluid interface is preserved in the slope of the rutile-titanite interface. Preferred dissolution occurs at the edges of some solitary titanite crystals.

titanite and at the titanite-rutile interface must be very different. Because titanite grows at the titanite-fluid interface (Fig. 6a), only some part of the Ti is fixed at the rutile-titanite interface. Titanium is transported from the location of rutile dissolution to the titanite-fluid interface, where it reacts immediately with the nearly Ca- and Si-saturated fluid to form titanite, and the Ti content of the bulk fluid remains very low. Transport of Ca and Si to the titanite-titanite and rutile-titanite interfaces is not sufficient to fix all dissolved Ti there, which requires a different composition of the fluid serving as a transport medium along the grain boundaries compared to that of the bulk fluid.

In the Si-undersaturated Al-system, we observed both polycrystalline titanite overgrowths and occasional solitary crystals on the rutile-fluid interface. A significant part of the rutile surface is exposed around the titanite crystals (Fig. 4a), i.e., fluid access to the Ti source was not restricted in these experiments in contrast to those cases where a spatially continuous titanite overgrowth was produced. The growth mechanism of solitary titanite crystals is therefore simple (Fig. 6b). The exposed rutile surface surrounding these crystals served as the Ti source and the rutile covered by titanite was protected from (or less prone to) dissolution, i.e., Ti was supplied largely from the rutile-bulk fluid interface. The exposed rutile surface is dissolved preferentially around solitary titanite (Fig. 4); where the rutile surface is "shielded" by titanite, dissolution is less pronounced. Sculpture on the exposed rutile surface is smooth and indicates, despite emphasizing growth steps and striations on the rutile, uniform dissolution during the reaction with the bulk fluid.

Comparison with dissolution patterns in a natural titanite–rutile reaction rim and concluding remarks

A natural example of titanite overgrowth on rutile formed during retrogression from eclogite facies to amphibolite facies conditions under fluid influx has been described previously (Lucassen et al. 2010a, 2011). Here, the growth of titanite occurred under static conditions similar to our experiments, and the corona texture lacks any deformation features. On a large single crystal of rutile, two different growth forms of titanite are observed (Fig. 7a): a polycrystalline titanite overgrowth, which is restricted to the contact of the rutile with its host amphibolite, and a large single crystal of titanite at the contact with a vein. The vein consists of coarse-grained hornblende-plagioclase with calcite and quartz. The two growth forms left distinct imprints of the rutile surface, and neither is related to the crystal orientation of the rutile. The polycrystalline titanite imposed a hump-and-valley morphology on the rutile surface (Fig. 7b) similar to the experimentally produced patterns, despite the much longer time frame and certainly extended cooling from the thermal peak in the natural sample. The preferred pathways for dissolution of the rutile beneath the titanite and element transport through the titanite rim must also have been the titanite grain boundaries. The trace left by the single-crystal titanite on the rutile surface (Fig. 7c) reflects the lozenge-shaped crystal morphology of the titanite. Titanite has a good cleavage on {110}, a poor cleavage on {111}, and twinning on {100} (Tröger 1982). The pattern observed on the rutile surface is interpreted to arise from preferential dissolution beneath these planes in the titanite crystal, i.e., to have developed largely independently of the crystallographic orientation of the rutile. The cleavage and twin planes obviously acted as pathways for element transport.

In the fluid-saturated system in our experiments, the dissolution of rutile and formation of titanite were fast. Even though we did not monitor the rate of dissolution, the incisions up to ~50 µm in depth indicate that at least 5% of the initial thickness of the rutile (1000 µm) has been removed within 30 days. Figure 5 shows only one crystal face, but the dissolution process was similar on all faces of the synthetic rutile. The dissolution patterns observed on the natural rutile are similar to those seen in our experiments, suggesting the same transport mechanism. Considering the fast dissolution rate in our experiments and the preservation of rutile with titanite overgrowth on the geological timescale, dissolution of rutile in natural systems must be substantially slower than in the fluid-saturated experiments. This difference could be explained by restricted availability of fluid in natural systems (e.g., formation of titanite during a fluid pulse where a significant proportion of the fluid is consumed by the newly formed hornblende in the natural sample).

We conclude from our study that the type of titanite overgrowth and the evolution of crystal morphology in the polycrystalline titanite with time control the geometry of the dissolution-precipitation front by fluid-enhanced transport. The rate-limiting process for dissolution of rutile and element transport is the availability of a fluid at the rutile-titanite interface inferred from the observation of enhanced dissolution of rutile beneath titanite grain boundaries. Fluid-assisted diffusion along grain boundaries, which depends on the amount and nature of available fluid, but also on the formation of other minerals in the same paragenesis, is one of the most important processes in metamorphic reactions. At completely static conditions, as in our experiments, the grain boundaries are the dominant pathways for element transport. Other possible pathways for the fluid are cleavage planes and twin boundaries, as in the natural sample

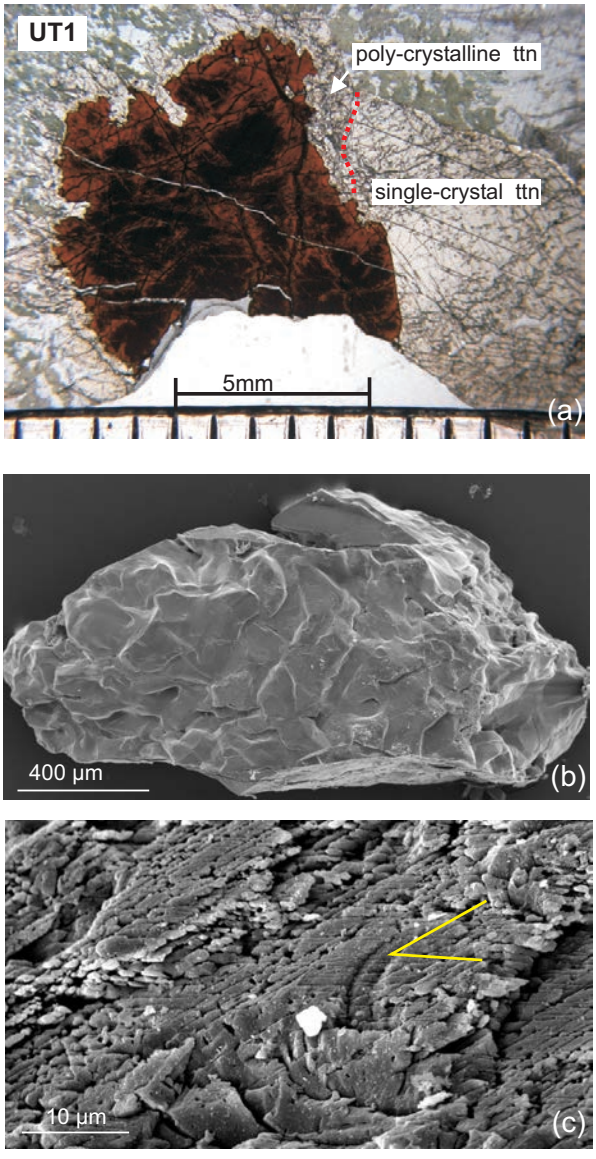

FIGURE 7. Natural titanite overgrowth and dissolution patterns on rutile from eclogite retrogressed at amphibolite facies conditions (sample UT1; Lucassen et al. 2010a, 2011). (**a**) Thin-section microphotograph (plane-polarized light) showing a polycrystalline (left and upper part, in contact with the amphibolite matrix) and single-crystal overgrowth of titanite on a rutile crystal (right, in contact with a vein with large plagioclase and amphibole). (**b**) SEM image of the rutile surface, after dissolution of the polycrystalline titanite, sculptured with a hump-and-valley pattern. (**c**) SEM image of the rutile surface beneath the single-crystal titanite, with an imprint of the lozenge-shaped outline of the titanite crystal (indicated by yellow lines) on the rutile.

described by Lucassen et al. (2010a, 2011). To our knowledge, the present report is the first example where the front of a fluid-mediated mineral reaction was documented in 3D. In the case studied here, the newly formed mineral has a dominating influence on the formation of a reaction corona and thus, there is a feedback between the products and educts.

The observations summarized above are potentially useful for other reactions. Further examples, which might be studied by the method of dissolution with HF applied here, are reaction coronas of silicates around corundum or spinel, promising to provide a better insight into overgrowth-controlled dissolution behavior of minerals that become unstable during retrogression. Examples below list such reactions in metamorphic rocks, involving an oxide mineral together with a fluid saturated in Si and other cations and resulting in a corona around the precursor oxide, or leaving relict inclusions in the newly formed silicate mineral:

ilmenite → titanite (e.g., Harlov et al. 2006);
corundum → sillimanite (e.g., Kelley and Harley 2004);
corundum → sapphirine + sillimanite (e.g., Santosh and Sajeev 2006);
spinel → sapphirine (e.g., Kriegsman and Schuhmacher 1999);
hercynite → cordierite (Heimann et al. 2006);
magnetite → staurolite/chloritoid (Barrientos and Selverstone 1987);
magnetite → titanite (Grew et al. 1989);
Zn spinel → staurolite (Stoddard 1979);
Cr spinel → Cr-epidote (Sánchez-Viscaíno et al. 1995);
högbomite → cordierite (Petersen et al. 1989);
chrysoberyl → beryl (Grundmann and Morteani 1995).

Note that Stoddard (1979) described the breakdown of staurolite to Zn-bearing spinel, but the reverse reaction would fit into the scheme of oxide-silicate reaction. Barrientos and Selverstone (1987) did not give details on the reaction textures involving magnetite and staurolite/chloritoid, but their descriptions led to the conclusion that such reactions did, in fact, take place. In all other examples listed above, typical reaction coronas or relicts of oxides in silicates are present, and these reactions require a similar mechanism involving dissolution of the precursor oxide and transport of the dissolved species through the reaction rim and/or transport of Si plus other cations to the reaction site. The reaction morphology on the partly dissolved oxides can provide important information on the location of fluid pathways in the rim. However, it should be noted that the solubility of these oxides, as well as the behavior and mobility of different dissolved species, may vary strongly under different *P-T-X* conditions. For example, in the case of ilmenite conversion to titanite, described by Harlov et al. (2006), Fe minerals were not observed in the reaction corona, indicating that all of the Fe derived from the precursor ilmenite was transported through the reaction rim into the surrounding rock matrix.

Acknowledgments

We thank Helga Kemnitz and Ilona Schäpan (both Deutsches Geoforschungszentrum) and Jörg Nissen (Zentraleinrichtung Elektronenmikroskopie, Technische Universität Berlin) for their invaluable help with the SEM, Irene Preuss (Zentraleinrichtung Elektronenmikrospie) for help with microphotography, and Christa Zecha (Technische Universität Berlin) for sample preparation. We thank Frank Spear and an anonymous referee for their helpful comments and Anton Chakhmouradian for excellent editorial handling and comments. This work was carried out as part of the research group FOR 741 "Nanoscale processes and geomaterials properties," sponsored by DFG code number DR DFG grant DR 744/3-1 and grant FR 557/26-2.

References cited

Antignano, A. and Manning, C.E. (2008) Rutile solubility in H_2O, H_2O–SiO_2, and H_2O–$NaAlSi_3O_8$ fluids at 0.7–2.0 GPa and 700–1000 °C: Implications for mobility of nominally insoluble elements. Chemical Geology, 255, 283–293.

Aranovich, L.Y. and Newton, R.C. (1996) H_2O activity in concentrated NaCl solutions at high pressures and temperatures measured by the brucite-periclase equilibrium. Contributions to Mineralogy and Petrology, 125, 200–12.

Audétat, A. and Keppler, H. (2005) Solubility of rutile in subduction zone fluids, as determined by experiments in the hydrothermal diamond anvil cell. Earth and Planetary Science Letters, 232, 393–402.

Ayers, J.C. and Watson, E.B. (1993) Rutile solubility and mobility in supercritical aqueous fluids. Contributions to Mineralogy and Petrology, 114, 321–330.

Barrientos, X. and Selverstone, J. (1987) Metamorphosed soils as stratigraphic indicators in deformed terranes: an example from the Eastern Alps. Geology, 15, 841–844.

Brewer, T.S., Storey, C.D., Parrish, R.R., Temperley, S., and Windley, B.F. (2003) Grenvillian age decompression of eclogites in the Glenelg-Attadale Inlier, NW Scotland. Journal of the Geological Society of London, 160, 565–574.

Fockenberg, T., Burchard, M., and Maresch, W.V. (2006) Experimental determination of the solubility of natural wollastonite in pure water at pressures of 5 GPa and at temperatures of 400 to 800°C. Geochimica et Cosmochimica Acta, 70, 1796–1806.

Grew, S.E., Asami, M., and Makimoto, H. (1989) Aluminous and manganoan titanite from the Sør Rondane Mountains, East Antarctica. Antarctic Journal of the United States, 24, 42–43.

Grundmann, G. and Morteani, G. (1995) Ein neues Vorkommen von Smaragd, Alexandrit, Rubin und Saphir in einem Topas-führenden Phlogopit-Fels von Poona, Cue District, West-Australien. Zeitschrift der Deutschen Gemmologischen Gesellschaft, 44, 11–31.

Harlov, D., Tropper, P., Seifert, W., Nijland, T., and Förster, H.-J. (2006) Formation of Al-rich titanite ($CaTiSiO_4O$–$CaAlSiO_4OH$) reaction rims on ilmenite in metamorphic rocks as a function of f_{H_2O} and f_{O_2}. Lithos, 88, 72–84.

Heimann, A., Spry, P.G., Teale, G.S., and Jacobson, C.E. (2006) Coronas, symplectitic textures, and reactions involving aluminous minerals in gedrite-cordierite-garnet gneiss from Evergreen, Front Range, Colorado. The Canadian Mineralogist, 44, 1025–1044.

Joachim, B., Gardés, E., Abart, R., and Heinrich, W. (2011) Experimental growth of åkermanite reaction rims between wollastonite and monticellite: evidence for volume diffusion control. Contributions to Mineralogy and Petrology, 161, 389–399.

Keller, L.M., Abart, R., Wirth, R., Schmid, D.W., and Kunze, K. (2006) Enhanced mass transfer through short-circuit diffusion: Growth of garnet reaction rims at eclogite facies conditions. American Mineralogist, 91, 1024–1038.

Kelley, N.M. and Harley, S. (2004) Orthopyroxene–corundum in Mg–Al-rich granulites from the Oygarden Islands, East Antarctica. Journal of Petrology, 45, 1481–1512.

Kriegsman, L.M. and Schuhmacher, J.C. (1999) Petrology of sapphirine-bearing and associated granulites from Central Sri Lanka. Journal of Petrology, 40, 1211–1239.

Lasaga, A.C. (1995) Fundamental approaches in describing mineral dissolution and precipitation rates. In A.F. White and S.L. Brantley, Eds., Chemical Weathering Rates of Silicate Minerals, 31, p. 23–86. Reviews in Mineralogy, Mineralogical Society of America, Chantilly, Virginia.

Lucassen, F., Dulski, P., Abart, R., Franz, G., Rhede, D., and Romer, R.L. (2010a) Redistribution of HFSE elements during rutile replacement by titanite. Contributions to Mineralogy and Petrology, 160, 279–295.

Lucassen, F., Franz, G., Rhede, D., and Wirth, R. (2010b) Ti-Al zoning of experimentally grown titanite in the system CaO-Al_2O_3-TiO_2-SiO_2-NaCl-H_2O-(F)—evidence for small scale fluid heterogeneity. American Mineralogist, 95, 1365–1378.

Lucassen, F., Franz, G., Dulski, P., Romer, R.L., and Rhede, D. (2011) Element and Sr isotope signatures of titanite as indicator of variable fluid composition in hydrated eclogite. Lithos, 121, 12–24, DOI: 10.1016/j.lithos.2010.09.018.

Manning, C.E., Wilke, M., Schmidt, C., and Cauzid, J. (2008) Rutile solubility in albite-H_2O and $Na_2Si_3O_7$-H_2O at high temperatures and pressures by in-situ synchrotron radiation micro-XRF. Earth and Planetary Science Letters, 272, 730–737.

Müller, W.F. and Franz, G. (2004) Unusual deformation microstructures in garnet, titanite and clinozoisite from an eclogite of the Lower Schist Cover, Tauern Window, Austria. European Journal of Mineralogy, 16, 939–944.

Newton, R.C. and Manning, C.E. (2006) Solubilities of corundum, wollastonite and quartz in H_2O-NaCl solutions at 800 °C and 10 kbar: Interaction of simple

minerals with brines at high pressure and temperature. Geochimica et Cosmochimica Acta, 71, 5571–5582.
Petersen, E.U., Essene, E.J., Peacor, D.R., and Marcotty, L.A. (1989) The occurrence of högbomite in high-grade metamorphic rocks. Contributions to Mineralogy and Petrology, 101, 350–360.
Putnis, A. (2009) Mineral replacement reactions. In E.H. Oelkers and J.Schott, Eds., Thermodynamics and Kinetics of Water-rock Interaction, 70, p. 87–124. Reviews in Mineralogy and Geochemistry, Mineralogical Society of America, Chantilly, Virginia.
Rapp, J.F., Klemme, S., Butler, I.B., and Harley, S.L. (2010) Extremely high solubility of rutile in chloride and fluoride-bearing metamorphic fluids: An experimental investigation. Geology, 38, 322–326.
Rötzler, J., Romer, R.L., Budzinski, H., and Oberhänsli, R. (2004) Ultrahigh-temperature granulites from Tirschheim, Saxon Granulite Massif, Germany: *P-T-t* path and geotectonic implications. European Journal of Mineralogy, 16, 917–937.
Sánchez-Viscaíno, V.L., Franz, G., and Gómez-Pugnaire, M.T. (1995) The behavior of Cr during metamorphism of carbonate rocks from the Nevado-Filabride complex, Betic Cordilleras, Spain. The Canadian Mineralogist, 33, 85–104.
Santosh, M. and Sajeev, K. (2006) Anticlockwise evolution of ultrahigh-temperature granulites within continental collision zone in southern India. Lithos, 92, 447–464.
Stoddard, E.F. (1979) Zinc-rich hercynite in high-grade metamorphic rocks: a product of the dehydration of staurolite. American Mineralogist, 64, 736–741.
Tröger, W.E. (1982) Optische Bestimmung der gesteinsbildenden Minerale. Teil 1 Bestimmungstabellen, 5th edition, p. 188. E. Schweizerbart'sche Verlagsbuchhandlung (Nägele und Obermiller), Stuttgart.
Tropper, P. and Manning, C.E. (2005) Very low solubility of rutile in H_2O at high pressure and temperature, and its implications for Ti mobility in subduction zones. American Mineralogist, 90, 502–505.
Wirth, R. (2004) Focused Ion Beam (FIB): A novel technology for advanced application of micro- and nanoanalysis in geosciences and applied mineralogy. European Journal of Mineralogy, 16, 863–877.
——— (2009) Focused Ion Beam (FIB) combined with SEM and TEM: Advanced analytical tools for studies of chemical composition, microstructure and crystal structure in geomaterials on a nanometre scale. Chemical Geology, 261, 217–229.

Manuscript received November 17, 2010
Manuscript accepted January 6, 2012
Manuscript handled by Anton Chakhmouradian